Supporting Information

Takahashi et al. 10.1073/pnas.0914594107

SI Materials and Methods

Animal Experiment Ethics. Experiments were performed with the approval of the animal experiment ethics committee at the University of Tokyo (approval number 19-43, A21-6) according to the University of Tokyo guidelines for the care and use of laboratory animals.

Slice Culture Preparations. Entorhino-hippocampal organotypic slices were prepared from 7-day-old Wistar/ST rats (SLC) as previously described (1). Briefly, rat pups were anesthetized by hypothermia and decapitated. The brains were removed and placed in aerated, ice-cold Gey balanced salt solution supplemented with 25 mM glucose. Horizontal entorhino-hippocampal slices were made at a thickness of 300 μm by a vibratome (DTK-1500; Dosaka). They were placed on Omnipore membrane filters (JHWP02500; Millipore) and incubated in 5% CO_2 at 37 °C. The culture medium, composed of 50% MEM (Invitrogen), 25% Hanks balanced salt solution, 25% horse serum (Cell Culture Laboratory), and antibiotics, was changed every 3.5 days. Experiments were performed on days 7 to 11 in vitro. Although slice cultures are known to self-rewire and form abnormal connections that very rarely exist in normal conditions, such as CA1-to-CA1, CA1-to-CA3, and CA3–to–dentate gyrus connections (2, 3), these aberrant connections are not dominant in our slice culture preparations. ROTing, a synapse mapping technique described later, demonstrates that these abnormal connections are less than 0.5% of the total connections and that an overwhelming number of the connections project to their normal targets. This is probably because in our preparations, the entorhinal cortex is not dissected from slices of the hippocampal formation. Lesions of the entorhinal cortex are known to result in abnormal sprouting and reorganization of hippocampal networks in vivo and ex vivo (4, 5).

Ex Vivo Patch-Clamp Recordings. A slice was placed in a recording chamber perfused at 3 to 4 mL/min with artificial cerebrospinal fluid (aCSF), consisting of 127 mM NaCl, 26 mM $NaHCO_3$, 3.3 mM KCl, 1.24 mM KH_2PO_4, 1.0 mM $MgSO_4$, 1.0 to 1.2 mM $CaCl_2$, and 10 mM glucose at 30 to 32 °C. Whole-cell recordings were carried out simultaneously from two to four pyramidal cells. Patch pipettes (4–6 MΩ) were filled with 135 mM K-gluconate, 4 mM KCl, 10 mM Hepes, 10 mM phosphocreatine, 4 mM MgATP, 0.3 mM NaGTP, and 0.2% biocytin. Single units were extracellularly recorded in the loose-cell–attached mode with aCSF-filled pipettes. To examine whether the recorded neurons were synaptically connected, aCSF was modified to 2.2 mM K^+, 3.0 mM Mg^{2+}, and 3.6 mM Ca^{2+} to reduce spontaneous activity and enhance the reliability of synaptic transmission (6).

In Vivo Patch-Clamp Recordings. Male ICR mice (18–20 day old) were anesthetized with urethane (1.2–1.8 g/kg, i.p.). Animals were implanted with a metal head-holder and mounted on a custom-made stereotaxic fixture. A small craniotomy (approximately 1 mm^2) was made at 2.5 mm caudal to the bregma and 2.2 mm ventrolateral to the sagittal suture along the surface of the skull, and the dura was removed. Whole-cell recordings were obtained with the blind patch-clamp approach (7).

Data Acquisition. All electrophysiological recordings were carried out using MultiClamp 700B amplifiers (Molecular Devices). Signals were low-pass filtered at 2 kHz and digitized at 20 kHz. Data were analyzed with custom-written scripts in IgorPro 6 (Wavemetrics). Excitatory and inhibitory postsynaptic current (EPSC and IPSC, respectively) were recorded at clamped voltages of –90 mV and 0 mV, respectively. EPSGs and IPSGs were computed on the assumption that EPSCs were recorded at the reversal potential for inhibition and that IPSCs were recorded at the reversal potential for excitation.

Dynamic-Clamp Stimulation. CA3 PCs were stimulated with the dynamic-clamp conductance injection technique. Synaptic events were modeled based on conductance $g(t)$, and the command current signal $I(t)$ was computed as a function of $I(t) = g(t) \times [V(t) - E_{rev}]$ ($V(t)$, membrane potential; E_{rev}, reversal potential) under a real-time Linux environment and delivered into patch-clamped neurons at 20 kHz by a PCI-6024E data acquisition board (National Instruments). Conductance stimuli (30 s) consisted of a series of excitatory synaptic inputs, which were constructed from 200 Poisson spike trains convolved with a unitary conductance transient representing a fast excitatory synaptic response fitted by the dual exponential function ($g_0 \times [\exp(-t/\tau_d) - \exp(-t/\tau_r)]$), where τ_r represents an activation time constant, τ_d a decay time constant, and g_0 a scaling factor ($\tau_r = 0.5$ ms, $\tau_d = 2$ ms, and $g_0 = 1{,}000$ pS). The average rate of the total input firing was 800 Hz. Two partially correlated conductance sweeps were simultaneously generated so that their correlation coefficient C_{in} ranged from 0 to 1 at roughly every 0.2 step; for an expected correlation level (c), two sweeps, $g_1(t)$ and $g_2(t)$, were constructed by overlapping $(1 - c) \times 200$ Poisson trains. To make the scaled synaptic input sweep, presynaptic spikes were distributed in a power law across trains. During stimulation, intrinsic fast synaptic transmission was blocked in the presence of an inhibitor mixture of 20 μM 6-cyano-7-nitroquinoxoxaline-2,3-dione, 50 μM D,L-2-amino-5-phosphonopentanoic acid, and 50 μM picrotoxin.

fMCI. Slices were incubated with 2 mL dye solution at 37 °C for 1 h (8). The dye solution was aCSF containing 0.0005% Oregon Green 488 BAPTA-1 (OGB-1) AM, 0.01% Pluronic F-127, and 0.005% Cremophor EL. After 1 h recovery, a slice was transferred to a recording chamber. Images were acquired at 500 to 2,000 frames per s with a Nipkow-disk confocal unit (CSUX-1; Yokogawa Electric), a high-speed back-illuminated CCD camera (iXon DU860; Andor), a water-immersion objective lens (magnification ×16, 0.80 NA; Nikon), and Solis software (Andor). Fluorophores were excited at 488 nm with an argon laser (10–15 mW, 532-BS-AO4; Omnichrome) and visualized with a 507-nm long-pass emission filter. In each cell body, the fluorescence change $\Delta F/F$ was calculated as $(F_t - F_0) / F_0$, where F_t is the fluorescence intensity at frame time t, and F_0 is baseline. Spike timings were determined as the onsets of individual Ca^{2+} transients with an automatic machine-learning algorithm that can accurately detect the timings within one-frame-jitter errors (9).

Local Field Potential Recordings and Ripple Detection. In some experiments, CA1 local field potentials were recorded during fMCI monitoring of the calcium activity of CA3 neurons. Glass pipettes were filled with 2 M NaCl and placed in CA1 stratum pyramidale. To extract the ripple wave activity, the recorded data were band-pass filtered at 150 to 300 Hz. Ripple-like events were automatically detected based on their oscillatory powers and durations; the root mean square (3-ms window) of the band-passed signal was used to detect the ripple wave with a power threshold of 5 SDs with 10 ms in duration.

ROTing. The ROTing technique was used to find synaptically coupled neurons located in an fMCI-imaged region (6). Immediately after monitoring spontaneous activity with fMCI, aCSF was modified to 2.2 mM K^+, 3.0 mM Mg^{2+}, and 3.6 mM Ca^{2+} to reduce spontaneous activity and the resultant plasticity of synaptic wiring that may occur. In slices loaded with OGB-1 AM, two CA3 or CA1 PCs were voltage-clamped at –70 mV, and 10 μM glutamate was locally puffed through iontophoretic pipettes (approximately 1 MΩ, 3–10 μA for each 1–5 s) to evoke spikes in a few CA3 neurons located in a fMCI-targeted region. The pipette was slowly moved over CA3 networks, and the evoked spikes were monitored by fMCI at 50 frames per s with an Andor DV897 CCD camera. These spike timings were statistically compared with EPSCs recorded in the patch-clamped neurons to determine the responsible presynaptic pyramidal neurons.

Nissl and Biocytin Staining. After each experiment, the slice was fixed in 4% paraformaldehyde overnight at 4 °C and 0.2% Triton X-100 overnight and then incubated overnight at 4 °C with NeuroTrace (N-21482, 1:100; Molecular Probes) or streptavidin–Alexa Fluor 594 conjugate (1:1,000; Invitrogen-Molecular Probes) for Nissl or biocytin staining, respectively. Based on biocytin staining, data obtained from PCs were selected to analyze patch-clamp data.

Surprise Index as Pairwise Correlation. We focused on pairwise spike correlations (10, 11), rather than higher-order correlations, because this study aimed to attribute spike synchronization to synaptic connection, i.e., a structural relationship between two neurons. Our high-speed scanning did not allow imaging for a period of more than 3 min, and the numbers of spontaneous spikes were often insufficient to precisely calculate the correlation coefficient (12). To estimate the pairwise similarity in our point-process dataset, therefore, we considered the probability that spikes can synchronize by chance. Synchronized spike pairs (SSPs), defined as any pairs of spikes that concurred in two neurons, were detected with a time window of 10 ms. If neuron$_i$ and neuron$_j$ are independent units that fire in a random manner, the probability $P(n)$ that they exhibit n SSPs during the observation period t is given by the Poisson equation:

$$P_{i,j}(n) = \frac{m_{i,j}^n}{n!} e^{-m_{i,j}}$$

where $m_{i,j}$ is the expected number of SSPs, i.e., $f_i \times f_j \times t$, and f_i and f_j denote the spike rates of neuron$_i$ and neuron$_j$, respectively. When SSPs occur n times, the probability (i.e., rareness) is:

$$\bar{P}_{i,j} = \sum_{k=n}^{\infty} P_{i,j}(k) = 1 - \sum_{k=0}^{n-1} P_{i,j}(k).$$

The surprise index ($S_{i,j}$) was defined as follows (13):

$$-\log_2 \bar{P}_{i,j}.$$

For extremely synchronized pairs with an S of more than 100 bits, S is denoted as 100 bits to avoid arithmetic precision problems in computing floating-point numbers.

Data Representation. We reported all averaged values as means ± SDs.

1. Koyama R, et al. (2007) A low-cost method for brain slice cultures. *J Pharmacol Sci* 104: 191–194.
2. De Simoni A, Griesinger CB, Edwards FA (2003) Development of rat CA1 neurones in acute versus organotypic slices: Role of experience in synaptic morphology and activity. *J Physiol* 550:135–147.
3. Gähwiler BH, Capogna M, Debanne D, McKinney RA, Thompson SM (1997) Organotypic slice cultures: A technique has come of age. *Trends Neurosci* 20:471–477.
4. Laurberg S, Zimmer J (1981) Lesion-induced sprouting of hippocampal mossy fiber collaterals to the fascia dentata in developing and adult rats. *J Comp Neurol* 200:433–459.
5. West JR, Dewey SL (1984) Mossy fiber sprouting in the fascia dentata after unilateral entorhinal lesions: Quantitative analysis using computer-assisted image processing. *Neuroscience* 13:377–384.
6. Sasaki T, Minamisawa G, Takahashi N, Matsuki N, Ikegaya Y (2009) Reverse optical trawling for synaptic connections in situ. *J Neurophysiol* 102:636–643.
7. Margrie TW, Brecht M, Sakmann B (2002) In vivo, low-resistance, whole-cell recordings from neurons in the anaesthetized and awake mammalian brain. *Pflugers Arch* 444:491–498.
8. Takahashi N, Sasaki T, Usami A, Matsuki N, Ikegaya Y (2007) Watching neuronal circuit dynamics through functional multineuron calcium imaging (fMCI). *Neurosci Res* 58:219–225.
9. Sasaki T, Takahashi N, Matsuki N, Ikegaya Y (2008) Fast and accurate detection of action potentials from somatic calcium fluctuations. *J Neurophysiol* 100:1668–1676.
10. Schneidman E, Berry MJ, 2nd, Segev R, Bialek W (2006) Weak pairwise correlations imply strongly correlated network states in a neural population. *Nature* 440: 1007–1012.
11. Shlens J, et al. (2006) The structure of multi-neuron firing patterns in primate retina. *J Neurosci* 26:8254–8266.
12. de la Rocha J, Doiron B, Shea-Brown E, Josić K, Reyes A (2007) Correlation between neural spike trains increases with firing rate. *Nature* 448:802–806.
13. Weaver W (1948) Probability, rarity, interest, and surprise. *Sci Mon* 67:390–392.
14. Humphries MD, Gurney K, Prescott TJ (2006) The brainstem reticular formation is a small-world, not scale-free, network. *Proc R Soc Lond B Biol Sci* 273:503–511.

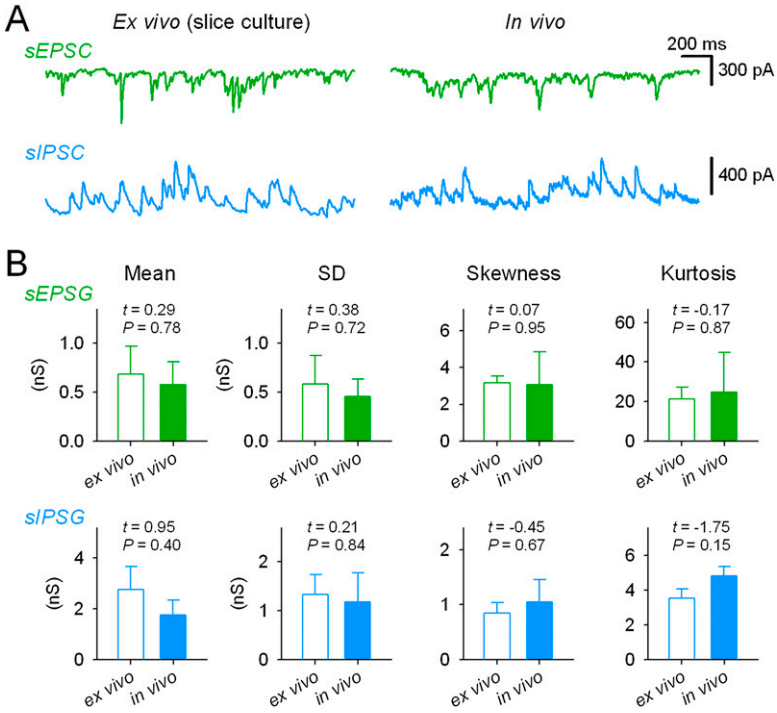

Fig. S1. Spontaneous synaptic activity in hippocampal slice cultures is similar to that in in vivo hippocampus. (*A*) Representative whole-cell patch-clamp traces of spontaneous excitatory postsynaptic current (*Upper:* sEPSC at –90 mV) and inhibitory postsynaptic current (*Lower*: sIPSC at 0 mV) recorded from hippocampal neurons in a slice culture preparation (ex vivo) and the hippocampus of a urethane-anesthetized mouse (in vivo). (*B*) We calculated the mean and SD as well as the third and fourth standardized moments, i.e., skewness, and kurtosis, of spontaneous excitatory postsynaptic conductance (*Upper*: sEPSG) and inhibitory postsynaptic conductance (*Lower*: sIPSG; n = 3 cells for each). No parameters did show statistical differences. Data are means ± SEM.

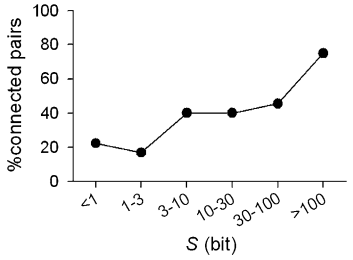

Fig. S2. The ratio of synaptic pairs increases as a function of *S*. CA3 PCs were randomly selected, and their spontaneous spike activities were recorded in current-clamp mode. The probability to find synaptically connected pairs were plotted against the spike synchronicity *S*.

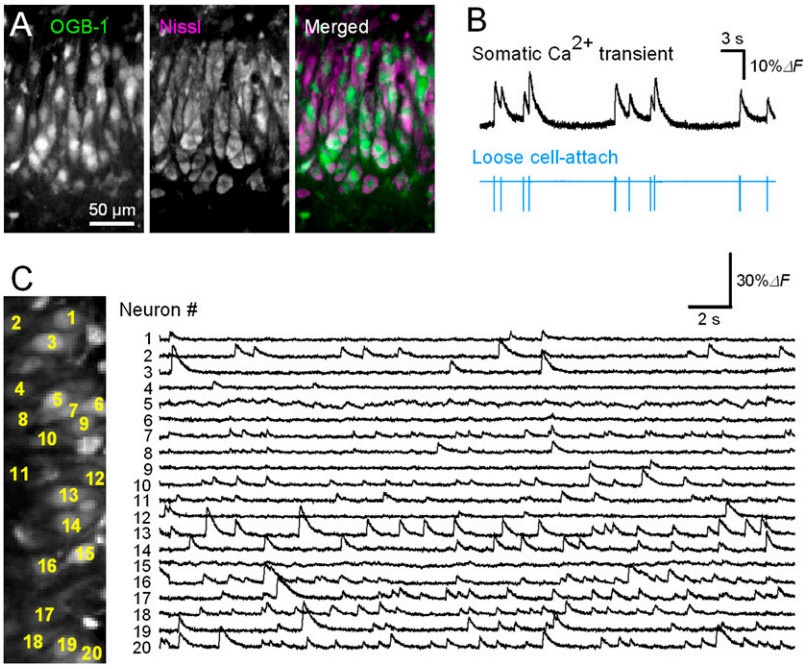

Fig. S3. High-speed fMCI. (*A*) Confocal images of the CA3 PC layer in an OGB-1 AM–loaded (*Left*) and post hoc Nissl–stained (*Center*) slice. Neurons are Nissl-positive and thus distinguishable from nonneuronal cells. (*B*) Simultaneous loose-patch recording and calcium imaging reveals that action potentials evoke somatic calcium transients. (*C*) Twenty neurons were monitored at 2,000 frames per s. Spontaneous $\Delta F/F$ traces of individual neurons (*Right*), the locations of which are also shown (*Left*).

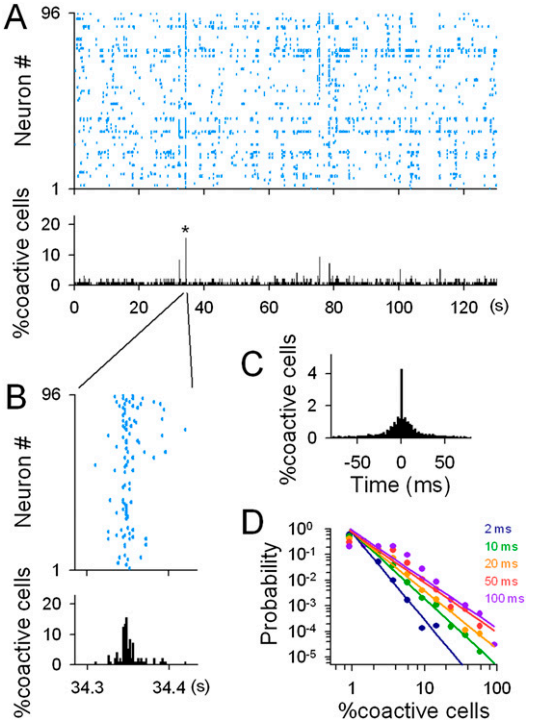

Fig. S4. Temporally sparse synchronization in spontaneously spiking CA3 networks. (*A*) (*Upper*) Rastergram of spontaneous spikes in 96 neurons monitored by fMCI (same as Fig. 3*A* in the main text). (*Lower*) Time histogram of the percentage of coactivated cells to the total imaged neurons (2-ms bin). (*B*) Time expansion of a single synchrony event marked by an asterisk in *A*. (*C*) Peri-synchronization time histograms in which the peak time of each synchrony event ($\geq 15 \times$ SDs from the mean activity) was aligned at time 0 ms (bin, 2 ms; $n = 985$ events of 14 slices). (*D*) Power-law distributions in synchrony size for various bin sizes (2, 10, 20, 50, and 100 ms) with the scaling exponents of −3.4, −2.6, −2.3, −2.0, and −1.9, respectively ($n = 14$ slices). The power law was robust for bin sizes of 2 to 100 ms.

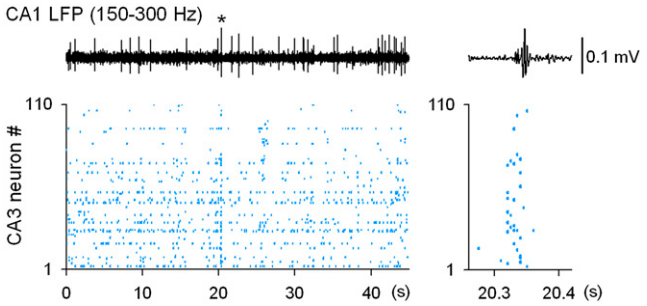

Fig. S5. Synchronization is accompanied by ripple-like high-frequency oscillations. Local field potentials (band-filtered at 150–300 Hz) were recorded from CA1 stratum radiatum (*Upper*), whereas CA3 network activity was monitored with fMCI (*Lower*). The event marked with an asterisk was magnified in time (*Right*). Ripple-like high-frequency oscillations occurred with CA3 network synchronization.

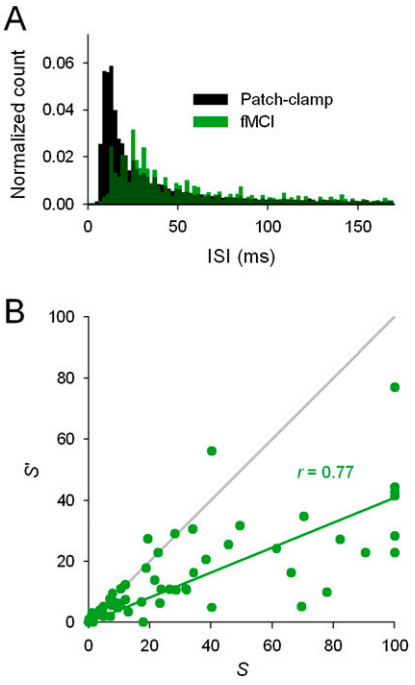

Fig. S6. Comparison of optically and electrophysiologically determined *S* values. (*A*) Distribution of interspike intervals in spontaneous activity of neurons recorded by whole-cell current-clamp technique (n = 154 cells; black) and high-speed fMCI (n = 1,193 cells; green). The latter often missed "bursty" spikes with intervals of less than 20 ms. (*B*) Relationship between *S* of intracellularly recorded neuron pairs and its modified value (*S'*) in which spikes in greater than 50-Hz burst firings, except for each first spike, were removed from the spike series. Each dot represents a single neuron pair. The gray line indicates the linear diagonal $S = S'$, and the green the linear least-square fit.

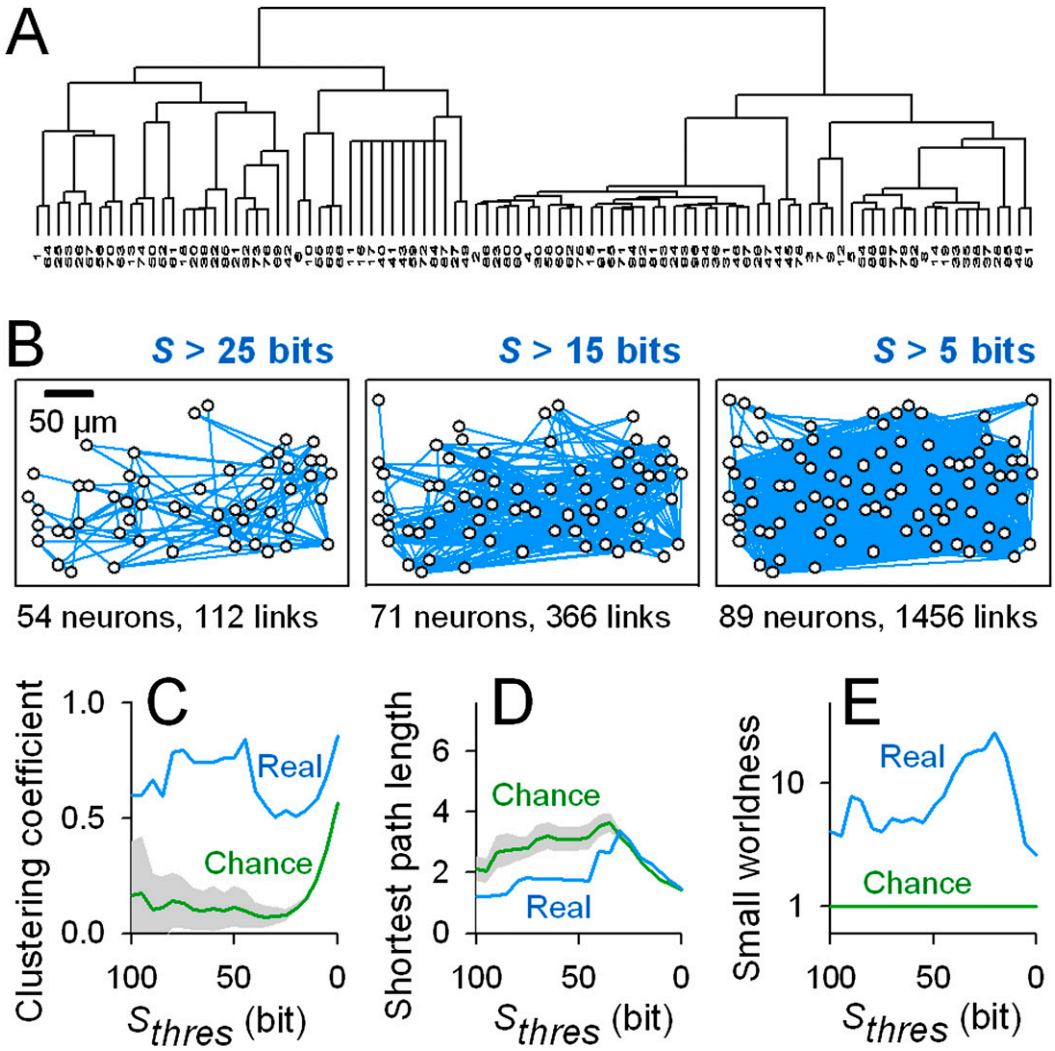

Fig. S7. Small-world architectures in synchrony-based connectivity. (*A*) The *S* matrix shown in Fig. 3*A* in the main text is hierarchically shown in a dendrogram format. (*B*) In the data for Fig. 3*A* in the main text, synchronized pairs were extracted at the *S* thresholds of 25, 15, and 5 (bits). Circles and lines in each graph indicate the extracted neurons and suprathreshold links, respectively. (*C* and *D*) Two metrics, i.e., the mean clustering coefficient *C* (a measure of how frequently neighbors of each cell are also neighbors of each other) and the mean shortest path length *L* (the average length of the shortest path between two cells), were compared with those of 200 equivalent random graphs. The random graphs maintained the total numbers of neurons and links, but all links were randomly rewired. Chance is represented as the mean (line) ± SD (shade) of 200 randomly rewired graphs. At any given *S* threshold, *C* was consistently larger than chance (C_{rand}), whereas *L* was close to chance (L_{rand}). (*E*) For a small-world network, the ratios $\lambda = L/L_{rand}$ and $\gamma = C/C_{rand}$ are expected to be approximately 1 and greater than 1, respectively. Therefore, we calculated the scalar measure of small-worldness, defined as γ/λ (14). The small-worldness was consistently higher than the chance level, i.e., 1, over the entire *S* threshold range.

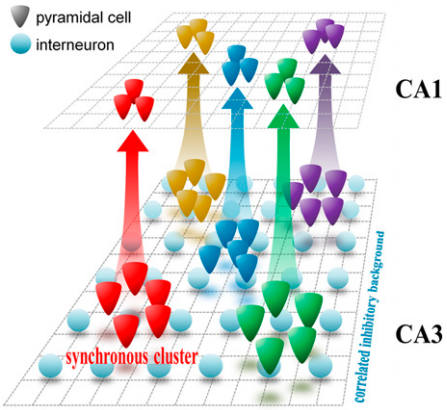

Fig. S8. Network organization and cell assemblies. The connectivity of CA3 PCs is densely clustered among specific neuron subsets (different colors). These interwired neurons thus receive correlated excitatory inputs and thereby generate highly synchronized spikes. CA3 inhibitory interneurons provide strongly correlated background inhibition, which may integrate CA3 PC groups. The synchronized CA3 spikes are specifically transmitted to subsets of CA1 PCs through relatively independent channels (arrows).

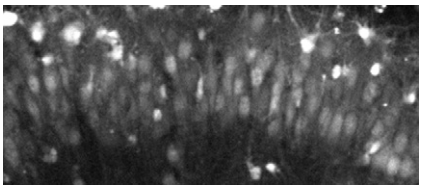

Movie S1. Spontaneous activity of CA3 neurons in a slice loaded with OGB-1 AM. Time is compressed by a factor of 2.

Movie S1